











## Roles of band gap and Kane electronic dispersion in the terahertz-frequency nonlinear optical response in HgCdTe

Davide Soranzio <sup>1,\*</sup>, Elsa Abreu <sup>1</sup>, Sarah Houver <sup>2</sup>, Janine Dössegger <sup>1</sup>, Matteo Savoini <sup>1</sup>, Frédéric Teppe <sup>3</sup>, Sergey Krishtopenko <sup>3</sup>, Nikolay N. Mikhailov <sup>4,5</sup>, Sergey A. Dvoretzky <sup>4,6</sup> and Steven L. Johnson <sup>1,7,†</sup>

<sup>1</sup>*Institute for Quantum Electronics, Eidgenössische Technische Hochschule (ETH) Zürich, CH-8093 Zurich, Switzerland*

<sup>2</sup>*Université Paris Cité, CNRS, Matériaux et Phénomènes Quantiques, F-75013, Paris, France*

<sup>3</sup>*Laboratoire Charles Coulomb, UMR CNRS 5221, University of Montpellier, 34095 Montpellier, France*

<sup>4</sup>*A.V. Rzhhanov Institute of Semiconductor Physics, Siberian Branch of Russian Academy of Sciences, Novosibirsk 630090, Russia*

<sup>5</sup>*Novosibirsk State University, Novosibirsk 630090, Russia*

<sup>6</sup>*Tomsk State University, Tomsk 634050, Russia*

<sup>7</sup>*Paul Scherrer Institut, 5232 Villigen, Switzerland*



(Received 17 April 2024; revised 14 August 2024; accepted 19 August 2024; published 3 September 2024)

Materials with linear electronic dispersion often feature high carrier mobilities and unusually strong nonlinear optical interactions. In this work, we investigate the (THz) nonlinear dynamics of one such material, HgCdTe, with an electronic band dispersion heavily dependent on both temperature and stoichiometry. We show how the band gap, carrier concentration and band shape together determine the nonlinear response of the system. At low temperatures, carrier generation from Zener tunneling dominates the nonlinear response with a reduction in the overall transmission. At room temperature, quasiballistic electronic dynamics drive the largest observed nonlinear optical interactions, leading to a transmission increase. Our results demonstrate the sensitivity of these nonlinear optical properties of narrow-gap materials to small changes in the electronic dispersion and carrier concentration.

DOI: [10.1103/PhysRevB.110.094303](https://doi.org/10.1103/PhysRevB.110.094303)

### I. INTRODUCTION

Materials such as graphene and topological semimetals with pseudo-relativistic band dispersion in the vicinity of the Fermi level have been reported to host a wide variety of interesting phenomena [1,2]. Some of these effects arise from the strong impact of the gapless electronic band dispersion and massless quasiparticles on the optical properties of the materials, which leads to strong nonlinear light-matter interactions such as carrier multiplication and high-order harmonic generation [3–5]. The relative importance of key parameters, such as the carrier concentration and small changes in the band gap of such materials in determining the nonlinear response, has at present not been well explored or understood, especially for interactions in the far infrared range (300 GHz–20 THz).

One example of a material with nearly linear electronic dispersion under certain conditions is bulk mercury cadmium telluride (MCT,  $\text{Hg}_{1-x}\text{Cd}_x\text{Te}$ ). MCT is an alloy of HgTe and CdTe commonly found in infrared detectors [6,7]. HgTe is a semimetal, while CdTe is a semiconductor with a band gap of 1.5 eV. The small lattice mismatch between the two compounds enables the synthesis of alloys with any value of doping  $x$  between 0 and 1 [8]. Near the  $\Gamma$  point, the electronic band structure of MCT can be described using a  $k \cdot p$  model [9]. The band gap in bulk MCT can be tuned to some extent and even eliminated using temperature [10],

biaxial strain [11], hydrostatic pressure [12], and randomly distributed impurities [13]. At regions of the phase diagram at the boundary between semimetallic and semiconducting phases, the electronic band structure shows a 3D linear dispersion of pseudo-relativistic quasiparticles called Kane fermions [10,14]. These quasiparticles share characteristics of ultrarelativistic Dirac fermions [15]. Unlike Weyl and Dirac semimetals, in MCT the band crossing is not topology- or symmetry-protected, although a  $\mathbb{Z}_2$  invariant can be defined to differentiate the phases.

In this work, we study the dynamics of a MCT film with  $x \approx 0.175$  using broadband 0.5–5 THz pulses, as a function of temperature and amplitude of the pulsed electric field. At this composition, MCT is a semiconductor with a band structure that changes strongly with temperature: as the temperature decreases, the band gap becomes narrower and the conduction band dispersion nearly linear. The change in band gap with temperature keeps the thermally activated carriers at relatively low concentrations across the whole temperature range [10]. This causes the equilibrium chemical potential to be close to the bottom of the conduction band for all temperatures. We use 1D and 2D broadband THz time-domain spectroscopies (TDS) [16] to investigate the low-frequency electrodynamic of this material in a transmission geometry.

We interpret our results by performing simulations using the finite-difference time-domain (FDTD) method [17]. We model carrier dynamics including the ballistic response and evaluating two different carrier generation mechanisms namely Zener tunneling [18] and impact ionization [19]. Finally, we compare the results of the experiments and

\*Contact author: [davideso@phys.ethz.ch](mailto:davideso@phys.ethz.ch)

†Contact author: [johnson@phys.ethz.ch](mailto:johnson@phys.ethz.ch)

simulations and discuss how band gap, carrier concentration and band shape determine the nonlinear response of the system. MCT serves as a model system for the interpretation of these phenomena, which can then be generalized to more complex narrow-band gap semiconductors.

## II. METHODS

### A. Experimental

The sample is a MCT heterostructure grown on a 400- $\mu\text{m}$ -thick semi-insulating (SI) GaAs substrate with lateral dimensions  $5 \times 3 \text{ mm}^2$  by the procedure described by Dvoretzky *et al.* [20]. Thin layers of CdTe, between 5–7  $\mu\text{m}$  thick, and ZnTe, approximately 30 nm thick, act as buffer layers between the substrate and the 3.2- $\mu\text{m}$ -thick (013) MCT film with doping  $x \approx 0.175$ , accompanied by two few-hundred-nm-thick MCT layers at its surfaces along the stacking direction with a monotonic increase of the Cd content to avoid stress and defects caused by a mismatch in the lattice parameters. More details regarding the sample structure can be found in Orlita *et al.* [14] and in Sec. I of Ref. [21]. For our measurements, the sample was mounted on a copper plate in front of a 2.7-mm circular hole and inserted into a helium cryostat.

The THz response was measured in two separate setups. Low-field, with peak values  $\approx 4 \text{ kV/cm}$ , 1D-TDS data were collected using a setup described previously by Suter *et al.* [22], focusing the THz beam to a diameter of 450  $\mu\text{m}$  at the sample position and using electro-optic detection of the THz waveform. A Ti:sapphire regenerative amplifier produces 50-fs full width at half maximum (FWHM) 800-nm pulses at a 250 kHz repetition rate. These pulses are split into two paths. One path directs the beam onto a spintronic emitter, generating quasi-single-cycle THz pulses which are then sent through the sample. The other beam path samples the transmitted electric field using electro-optic sampling in a 300- $\mu\text{m}$ -thick (110) GaP crystal.

A schematic of the high-field 2D-TDS setup is provided in Sec. II of Ref. [21]. In short, a laser system based on a Ti:Sapphire regenerative amplifier produces femtosecond pulses (800 nm, 100-fs FWHM, 1 kHz). A beamsplitter divides these pulses, which are then directed into a pair of three-stage optical parametric amplifiers (OPAs). The signal output from each OPA is individually tuneable to wavelengths near 1.5  $\mu\text{m}$ . Mechanical choppers inserted into the two signal outputs create pulse trains at submultiples of the 1 kHz laser repetition rate: one at 500 Hz (beam 1) and the other at 250 Hz (beam 2). To create THz-frequency pulses, each beam is then focused into a crystal of 4-N,N-dimethylamino-4'-N'-methyl-stilbazolium 2,4,6-trimethylbenzenesulfonate (DSTMS). Optical rectification of the pulses creates broadband THz radiation centered at approximately 2 THz [23]. For each beam a pair of wire-grid polarizers controls the electric field amplitude and polarization of the THz pulses. The pulses are then combined, directed toward the sample using plane mirrors and focused to a diameter of approximately 450  $\mu\text{m}$  (FWHM) with off-axis parabolic mirrors. A series of off-axis parabolic mirrors then refocuses the transmitted THz into a GaP electro-optic sampling crystal in combination with a small part of the 800-nm beam split

before the OPAs. The parameters of the GaP crystal are the same as in the 1D measurements. To estimate the peak fields and waveforms of the incident pulses, we remove the sample and measure the fields for each pulse train individually. The absolute field amplitudes are estimated using the relations found in Hirori *et al.* [24]. To reduce the contribution of the quadratic Kerr response, we inserted calibrated Si filters after the sample to reduce the field amplitude arriving at the GaP crystal until we observed a linear dependence of the field amplitude on additional attenuation.

The different chopping rates for the two beams allow to record quasimultaneously the transmitted signal for four distinct field combinations: both THz pulses [ $E_t(t)$ ], only one of the two pulses [ $E_1(t)$ ,  $E_2(t)$ ] and no THz pulse [ $E_b(t)$ , background]. For the measurements performed without the sample in place, we define  $E_{j,i}(t) = E_j(t) - E_b(t)$  as the “input” waveform, where  $j = t, 1, 2$ . We assume that the functions  $E_{j,i}$  are a good approximation of the incident electric field waveforms on the sample for the respective cases. For measurements with the sample in place, we define  $E_{j,o}(t) = E_j(t) - E_b(t)$  as the “output” waveform, where again the subscript  $k$  indicates which set of pulses is incident on the sample. Both beams enter the sample at normal incidence, with parallel electric field polarizations along the crystallographic [331] direction, as verified through Laue x-ray diffraction. The THz beam paths were maintained in a low-humidity environment ( $< 2\% \text{ RH}$ ) to minimize absorption by water vapor.

For each transmitted single-pulse waveform, we define the time centroid as

$$t_j = \int |E_{j,o}(t)|^2 dt / \int |E_{j,o}(t)|^2 dt \quad (1)$$

where  $j = 1, 2$  [25]. To describe the relative timing of the two pulses and the electro-optic sampling beam we also define two time coordinates: the excitation delay  $t_{\text{ex}} = t_2 - t_1$ , which is the difference between the time centroids, and the detection delay  $t_{\text{del}} = t - t_2$ , where  $t$  is the time probed by electro-optic sampling.

To isolate nonlinear effects, we define the “nonlinear” signal  $E_{\text{nl},o} = E_{t,o} - E_{1,o} - E_{2,o}$  and the “nonlinear-probe” signal  $E_{\text{nlp},o} = E_{t,o} - E_{1,o}$ , which depend on the temporal superposition of the individual fields. The typical waveforms of the THz pulses employed in the 1D- and 2D-TDS experiments can be found in Secs. III and IV of Ref. [21]. As shown in Appendix, we observed during the experiment that high peak fields can significantly modify the transmission and spectrum of even a single pulse. For this reason, we kept the peak field of pulse 2 to below 9 kV/cm, where such effects appear to be negligible. In this way we focus on the nonlinear response caused by higher fields in pulse 1.

### B. FDTD simulations

The numerical simulations were carried out based on the discretized version of Maxwell’s equations proposed by Yee [17], as described by Huber [26] following the scheme from Rumpf [27]. All fields are assumed to depend on only one spatial coordinate  $z$ , where  $z = 0$  defines the boundary between air and the sample. The local electric displacement field at a

time  $t$  can be written as

$$\mathbf{D}(z, t) = \epsilon_0 \epsilon_\infty(z) \mathbf{E}(z, t) + \mathbf{P}_e(z, t) + \mathbf{P}_{ph}(z, t), \quad (2)$$

where  $\epsilon_0$  is the vacuum permittivity,  $\epsilon_\infty(z)$  is the high-frequency relative permittivity of the medium at  $z$ ,  $\mathbf{E}(z, t)$  is the electric field,  $\mathbf{P}_e(z, t)$  the electronic polarization density and  $\mathbf{P}_{ph}(z, t)$  the polarization density from low-frequency infrared-active vibrations. Here we assume  $\mathbf{P}_e(z, t)$  includes only contributions from free carriers, and that contributions from other electronic transitions or high-frequency vibrational modes are included in  $\epsilon_\infty(z)$  and are time-independent. In our simulations we include the MCT layer, the two buffer layers (CdTe and ZnTe) and the GaAs substrate. We assume that  $\mathbf{P}_e(z, t) = 0$  for all materials except for the MCT layer and  $\mathbf{P}_{ph}(z, t) = 0$  for all materials except for the MCT and CdTe layers. The sample is modeled as a 1D succession of layers with different dielectric constants based on the composition profile reported in Refs. [14,20]. A detailed description can be found in Sec. I of Ref. [21].

To model the electronic polarization density  $\mathbf{P}_e(z, t)$ , we assume that the conduction band electrons with density  $n(z, t)$  behave as a quasiballistic wave packet with an average wave vector  $\mathbf{k}(z, t)$  [28]. The dynamics of  $\mathbf{P}_e(z, t)$  are then determined by

$$\frac{\partial \mathbf{P}_e(z, t)}{\partial t} = -en(z, t)\mathbf{v}[\mathbf{k}(z, t)] \quad (3)$$

where  $e$  is the fundamental charge,

$$\mathbf{v}(\mathbf{k}) = \frac{1}{\hbar} \nabla_{\mathbf{k}} \mathcal{E}(\mathbf{k}) \quad (4)$$

is the wave-packet group velocity,  $\hbar = h/2\pi$  with  $h$  Planck's constant and  $\mathcal{E}(\mathbf{k})$  is the energy of the conduction band at  $\mathbf{k}$ .

Regarding  $\mathcal{E}(\mathbf{k})$ , we use the electronic band structure for  $\text{Hg}_{0.825}\text{Cd}_{0.175}\text{Te}$  in an isotropic approximation, shown to be effective to describe its magnetoabsorption [10]. We estimate based on the data of Tepepe *et al.* [10] that the band gap varies between 9 and 138 meV over the temperature range 13 K to 300 K, approaching gapless linear dispersion at low temperatures. In such conditions, the band structure near the Fermi level can be described using an isotropic simplified Kane model [9] valid in the vicinity of the bottom of the  $\Gamma$  valley. The conduction band dispersion is expressed by the

$$\mathcal{P}(\mathcal{E}_n) = \frac{3.2 \times 10^7 V e^4 m_0^* [F_1 F_2]_0^2 \rho_v}{\epsilon_0^2 h^3 \epsilon_0^2} \int_1^{\mathcal{E}_n} dx \frac{(a^2 + 1)x^2 \{ [2(\mathcal{E}_n - x) + 1]^2 - 1 \}^{1/2} [2(\mathcal{E}_n - x) + 1][2x - 1] \{ [2x - 1]^2 - 1 \}^{1/2}}{a^2 + x^2 [(\lambda/k_g)^2 + x^2]}, \quad (8)$$

where  $\mathcal{E}_n = \mathcal{E}_c/\mathcal{E}_g$  is the ratio between the electron energy with respect to the bottom of the conduction band and the band gap,  $V$  is the unit cell volume [35],  $a = \sqrt{10}$  is a numerical value chosen to adjust the overlap integral  $[F_1 F_2]_0^2$  (values reported in Kinch [34]),  $\rho_v = (\mathcal{E}_g m_0^* m_{hh}^*/2)^{1/2} 8\pi/h^3$  is the density of states in the heavy-hole band [34],  $\epsilon_0$  is the low-frequency ( $\omega \rightarrow 0$ ) relative permeability from Baars

quasirelativistic relation [10]

$$\mathcal{E}_c(k) = -\mathcal{E}_g/2 + \sqrt{m_0^* \tilde{c}^4 + \hbar^2 k^2 \tilde{c}^2}, \quad (5)$$

where  $\mathcal{E}_g$  the electronic band gap,  $m_0^*$  is the effective mass at the bottom of the conduction band,  $\tilde{c}$  is the asymptotic velocity of Kane fermions (weakly dependent on temperature) and  $k$  is the wave-vector magnitude. Since  $m_0^* \tilde{c}^2 \approx \mathcal{E}_g/2$  [10],  $\mathcal{E}_c = 0$  corresponds to the bottom of the conduction band.

We now need to determine the wave vector of the wave packet  $\mathbf{k}(z, t)$ . In the ballistic regime, this is given by the equation of motion [29]

$$\hbar \frac{\partial \mathbf{k}(z, t)}{\partial t} + \gamma_P \hbar \mathbf{k}(z, t) = -e\mathbf{E}(z, t), \quad (6)$$

where  $\gamma_P$  is an electron scattering term. We assume that initially  $\mathbf{k}(z, t) = 0$ .

The carrier density  $n(z, t)$  is initially set at a value based on the temperature-dependent measurements of Tepepe *et al.* [10] (see also Sec. III in Ref. [21]). For the highest electric fields used in our experiments, however, we expect that the density of carriers may increase [29,30]. In the simulations, we tested two possible carrier generation mechanisms, namely Zener tunneling [18,31] and impact ionization [19,30].

The Zener interband tunneling effect has been observed in several narrow-gap semiconductors in the presence of a static electric field [18,32] and it has been previously reported for  $\text{Hg}_{1-x}\text{Cd}_x\text{Te}$  diodes [33]. Since the time steps in our simulation are much smaller than the field oscillation period, we can approximate the propagation of our THz pulses as a succession of constant-field steps. The instantaneous rate of carrier generation is then [18]

$$\left. \frac{\partial n(z, t)}{\partial t} \right|_{\text{Zener}} = \frac{e^2 E(z, t)^2}{18\pi \hbar^2} \left( \frac{m_\mu}{\mathcal{E}_g} \right)^{1/2} \exp\left( \frac{-\pi m_\mu^{1/2} \mathcal{E}_g^{3/2}}{2\hbar e |E(z, t)|} \right), \quad (7)$$

where  $E(z, t)$  is the local electric field magnitude,  $m_\mu = m_0^* m_{hh}^*/(m_0^* + m_{hh}^*)$  is the reduced mass, and  $m_{hh}^* = 0.55 \cdot m_e$  is the effective mass of the heavy-hole bands at the  $\Gamma$  point with  $m_e$  the electron rest mass (from Ref. [34], Chap. 7).

Impact ionization can be modelled based on the estimate of probability per unit time for impact ionization in MCT (Eq. 7.9, from Kinch [34])

and Sorger [36],  $\epsilon_0$  is the vacuum permeability,  $\lambda$  is the screening parameter of the Coulomb interaction, assumed to be negligible ( $\lambda = 0$ ) during impact ionization [34], and  $k_g = \sqrt{8m_0^* \mathcal{E}_g \pi^2 / \hbar^2}$  [34]. In order to take into account the momentum change of the electron wave packet due to the scattering event, we added to the left-hand side of Eq. (6) an effective damping force  $-\mathbf{F}_{\text{imp}}(\mathbf{k})$  following the procedure

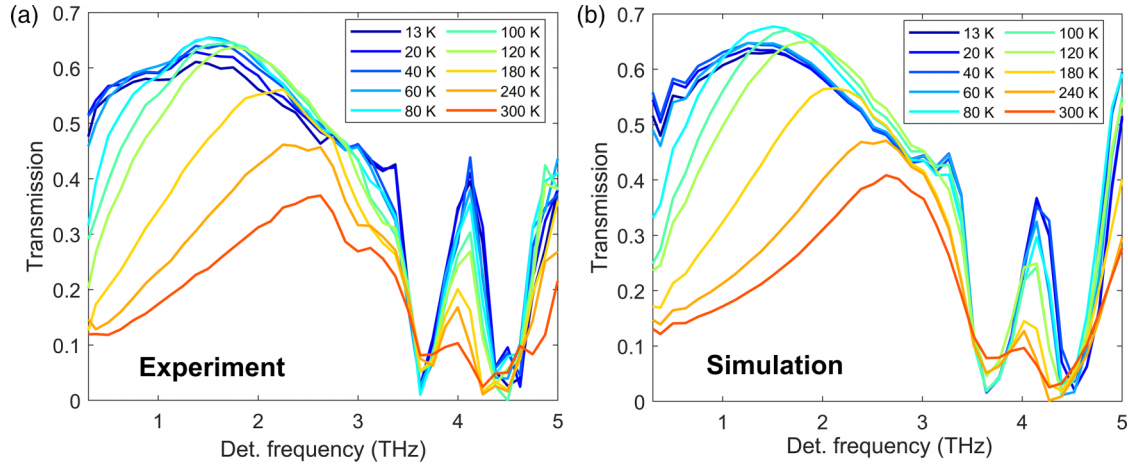


FIG. 1. Low field ( $\approx 4$  kV/cm) (a) experimental and (b) FDTD-simulated 1D-TDS transmission spectra of  $\text{Hg}_{0.825}\text{Cd}_{0.175}\text{Te}$  at different temperatures.

described by Biasco *et al.* [37], such that

$$\mathbf{F}_{\text{imp}} = \hbar \frac{\partial \mathbf{k}}{\partial t} \Big|_{\text{imp}} = -\frac{\hbar}{2} \frac{(1 + 2\alpha\mathcal{E}_c)(\mathcal{E}_c - \mathcal{E}_{\text{th}})\mathcal{P}(\mathcal{E}_n)}{(1 + \alpha\mathcal{E}_c)\mathcal{E}_c} \times \theta(\mathcal{E}_c - \mathcal{E}_{\text{th}})\mathbf{k}, \quad (9)$$

where  $\alpha = 1/\mathcal{E}_g$  [38] and we assumed  $\mathcal{E}_{\text{th}} \approx \mathcal{E}_g$  [30]. We can then write

$$\frac{\partial n(z, t)}{\partial t} \Big|_{\text{imp}} = \mathcal{P}[\mathcal{E}_n(z, t)]n(z, t). \quad (10)$$

In principle, we could now define a total rate of change for the carrier density by adding the contributions from Eqs. (7) and (10). In practice, we instead simulated scenarios where only one carrier generation mechanism was active.

Now we turn to the third term on the right-hand side of Eq. (5), the phonon-polariton contribution to the polarization density. We approximate MCT as having two phonon-polariton modes in our frequency range, so that  $\mathbf{P}_{\text{ph}}(z, t) = \mathbf{P}_1(z, t) + \mathbf{P}_2(z, t)$  and

$$\begin{aligned} \frac{\partial^2 \mathbf{P}_m(z, t)}{\partial t^2} + \Gamma_m \frac{\partial \mathbf{P}_m(z, t)}{\partial t} + \omega_{\text{TO},m}^2 \mathbf{P}_m(z, t) \\ = \varepsilon_\infty(z)(\omega_{\text{LO},m}^2 - \omega_{\text{TO},m}^2)\mathbf{E}(z, t), \end{aligned} \quad (11)$$

where  $\nu_{\text{LO},m} = \omega_{\text{LO},m}/2\pi$  and  $\nu_{\text{TO},m} = \omega_{\text{TO},m}/2\pi$  are the longitudinal and transversal frequencies and  $\gamma_m$  is the damping rate of the  $m$ -th mode. We assume that all polarization densities are initially zero. Further details can be found in Sec. I of Ref. [21].

### III. RESULTS

#### A. 1D-TDS

We first performed low-field 1D-TDS measurements at different temperatures to understand the linear response of the material. In Fig. 1(a), the transmission spectra of the sample are shown for a range of temperatures. As the sample is warmed up, a gradual increase of the carrier concentration leads to a change of the left slope of the spectrum together with an overall decrease of the transmission. A shallow dip

in the transmission appears close to 3.0 THz for higher temperatures, which has been observed in previous work [39–41]. The two dips around 3.6 and 4.4 THz have also been observed earlier and attributed to Hg-Te and Cd-Te vibrations, where the largest contributions come from modes which are both Raman- and IR-active [42,43].

Figure 1(b) shows the results of our simulation of the 1D-TDS, after adjusting the electron carrier concentration and scattering rate together with the longitudinal and transversal frequencies and scattering rate of the phonon-polariton terms. The complete set of parameters can be found in Sec. III of Ref. [21]. The simulations were performed including the contribution of Zener tunneling to carrier generation. For the lowest temperatures the best-fit parameters for the carrier concentration are close to the values reported by Tepe *et al.* [10], while at higher temperatures we observed that the best fit was found for concentrations of a factor approximately 2 lower.

The decrease in transmission as temperature grows is well-captured by the simulations. The two transmission minima above 3 THz are accurately reproduced in the simulations, where they arise from vibrational resonances. The shallow dip at approximately 3 THz seen at high temperatures is not captured by the simulations. This feature has been resolved before but has an unclear origin [39–41]. It may be related to additional vibrational resonances that we do not include in the model.

#### B. 2D-TDS

In Fig. 2, we report 2D-TDS maps at two different temperatures. To better understand the nature of the nonlinear signal, the three experimental datasets  $E_{1,o}$ ,  $E_{2,o}$ , and  $E_{t,o}$  are shown in panels (a)–(c) for  $T = 20$  K and peak  $E_{1,i} = 17$  kV/cm and  $E_{2,i} = 8$  kV/cm; using two pulses with comparable amplitudes here allows to distinguish their contributions to  $E_{t,o}$ . Panels (d) and (g) show the nonlinear probe  $E_{\text{nlp},o}$  at 20 and 300 K, respectively, with peak  $E_{1,i} = 169$  kV/cm and  $E_{2,i} = 8$  kV/cm as a function of excitation delay  $t_{\text{ex}}$  and detection delay  $t_{\text{del}}$ . The nonlinear probe can be roughly interpreted as the transmitted  $E_2$  field with respect to the arrival time of the  $E_1$  field. At 20 K,  $E_{\text{nlp},o}$  first oscillates, then quickly

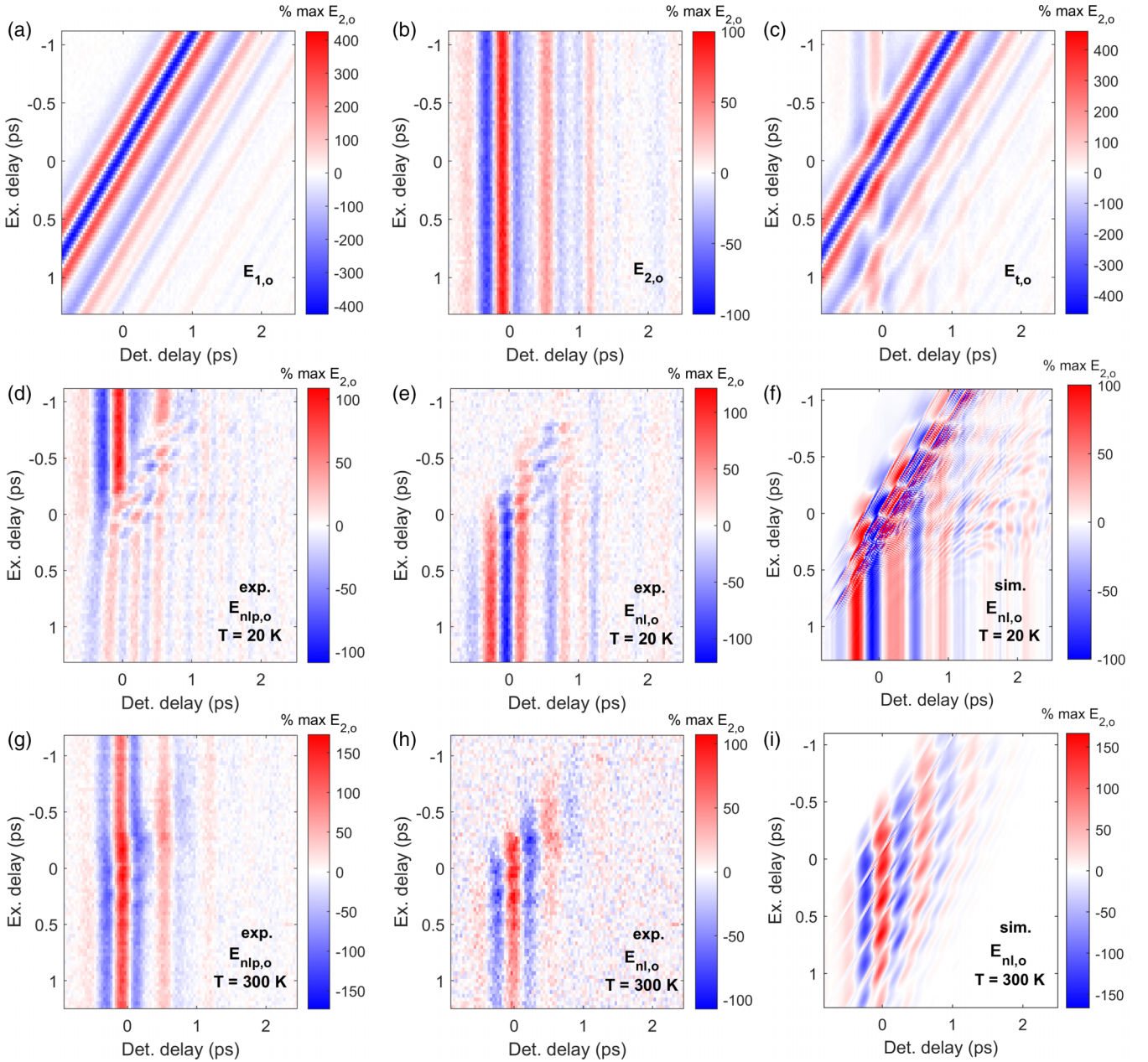


FIG. 2. 2D-TDS maps. [(a)–(c)] Measurements of (a)  $E_{1,o}$ , (b)  $E_{2,o}$  and (c)  $E_{t,o}$  acquired at  $T = 20$  K for peak fields  $E_{1,i} = 17$  kV/cm and  $E_{2,i} = 8$  kV/cm. (d) Experimental nonlinear probe  $E_{nlp,o}$  and (e) nonlinear  $E_{nl,o}$  signals recorded at  $T = 20$  K for peak fields  $E_{1,i} = 169$  kV/cm and  $E_{2,i} = 8$  kV/cm. The data presented in (e) can be directly compared with the FDTD-simulated  $E_{nl,o}$  in panel (f), using the same incident field amplitudes. [(g)–(h)] The experimental nonlinear probe  $E_{nlp,o}$  and experimental nonlinear  $E_{nl,o}$  signals measured at  $T = 300$  K and the same pulse field strengths as in (d) and (e). (i) The simulated  $E_{nl,o}$  at  $T = 300$  K, using the same incident field amplitudes as (h).

decreases by almost 80% after the arrival of  $E_1$ , remaining unchanged for excitation delays of several picoseconds (see Sec. V [21]). In contrast, at 300 K, we observe more extended oscillations around the pulse overlap region together with a slow increase in  $E_{nlp,o}$  that relaxes within a couple of picoseconds. A complementary view on the phenomenon is given by the nonlinear signal  $E_{nl,o}$  shown in panels (e) and (h) at 20 and 300 K, respectively. The evolution of the response as a function of the time delay between the two pulses can also be visualized taking constant detection-delay profiles as reported in Fig. 3 for two different peak amplitudes of  $E_{1,i}$

at  $T = 20$  K [panel (a)] and  $T = 300$  K [panel (b)]. In the  $T = 20$  K comparison, we observe that the modulation period decreases for higher peak field, in contrast to what observed for  $T = 300$  K. We have also taken 2D nonlinearity maps over somewhat longer excitation delay ranges for a selection of intermediate temperatures and input fields (Sec. V, [21]). For the higher peak fields  $E_{1,i}$  at  $T = 300$  K, these data show a slow decrease in  $E_{nlp,o}$  that emerges on a time scale that shortens with increasing field strength, down to approximately 5 ps at 169 kV/cm. These changes in  $E_{nlp,o}$  appear similar to the long-excitation-delay behavior of  $E_{nlp,o}$  seen at  $T =$

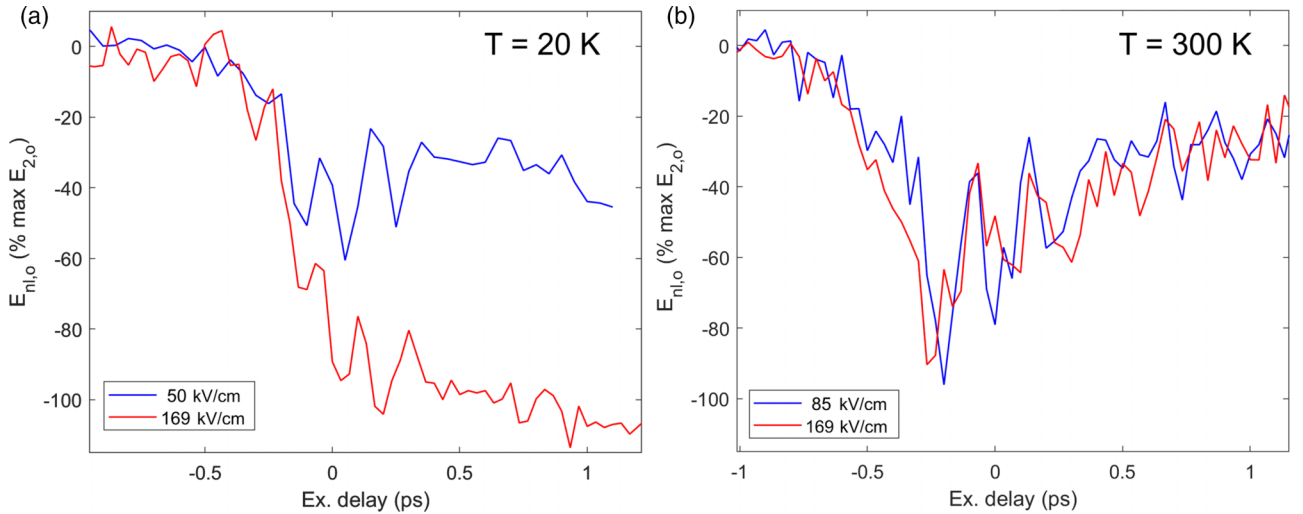


FIG. 3. Time-resolved excitation-delay profiles  $E_{nl,o}$  for peak  $E_{2,i} = 8$  kV/cm and two different  $E_{1,i}$  field amplitudes at constant detection delay averaged at (a)  $T = 20$  K ( $t_{del} = -0.06$  ps, in a  $\pm 50$  fs window) and (b)  $T = 300$  K ( $t_{del} = 0.23$  ps in a  $\pm 33$  fs window).

20 K at lower fields, but are much smaller in magnitude. We also observe changes in the single-pulse transmission as a function of field strength, which are summarized in Appendix.

For our simulations of the 2D nonlinear response, we use the electronic and vibrational parameters determined from adapting the 1D simulations to match our data, without further adjustment. We initially performed simulations assuming only Zener tunneling as a mechanism for carrier generation. The results shown in Fig. 2(f) and 2(i) capture the clear distinction between the  $T = 20$  and 300 K cases that we observe in the corresponding experimental maps [panels (e) and (h)]. At  $T = 20$  K, the simulations well reproduce the approximate magnitude of the nonlinear response as well as the behavior at long excitation delays (above 1 ps). In the region where the two pulses overlap in time, the simulation shows some high frequency modulations in the nonlinear signal along a diagonal direction, which does not appear in the experimental maps. We comment on this in Appendix. For  $T = 300$  K, the simulation reproduces the approximate overall magnitude and modulation seen in the experimental data, but has a significantly higher modulation visibility.

One interesting feature of the 2D maps is the change in behavior at long excitation delays as the temperature increases: at  $T = 20$  K, we see a drop in the transmission of pulse 2 that becomes nearly independent of excitation delay, whereas at  $T = 300$  K, we see a relaxation on a time scale of about 1 ps. To study this aspect of the data in more detail, we acquired constant-excitation-delay traces at  $t_{ex} = 2.54$  ps, averaged over a  $\pm 67$  fs range, as a function of both temperature and peak field  $E_{1,i}$ . In Fig. 4(a), we show the maximum value of the measured nonlinear signal  $E_{nl,o}$  over our detection delay range as a function of temperature for different peak fields of pulse 1. For comparison we also show the results of our simulation. For all peak field values, we see that the nonlinear signal increases with decreasing temperature, with an apparent threshold temperature where the effects become quite strong. For the highest fields we observe a saturation in the nonlinear response that is also reproduced quite accurately

by the simulations. Figure 4(b) shows the maximum nonlinear signal as a function of peak field at  $T = 20$  K. Here we also show the results of the simulations with Zener tunneling and impact ionization individually as the only carrier generation mechanism. We see here that while the simulation of Zener tunneling fairly accurately describes the magnitude and saturation of the nonlinear response at high fields, the simulation of impact ionization severely underestimates the magnitude of the nonlinearity and does not reproduce the saturation behavior seen in the experiment.

In addition to examining the behavior of the maximum of the nonlinear effect at long excitation delays, we can also study the dependence of the nonlinear probe signal on the detection delay. Figure 5 shows the full  $E_{nlp,o}$  trace as a function of detection delay associated with the data summarized Fig. 4(b). Panel (a) shows the gradual reduction of the pulse transmission as the  $E_{1,i}$  field amplitude grows. This change is accompanied by a modification of the relative spectral weight of the transmitted frequency components, leading to an approximately 3 THz oscillation for high fields. The simulated counterpart (using Zener tunneling) is reported in panel (b). The transmission of the  $E_{2,i}$  field decreases as the  $E_{1,i}$  field increases and the best quantitative correspondence is found for intermediate fields. As with the experimental data, at high  $E_{1,i}$  field amplitudes the spectral content of the transmitted pulse shifts towards higher frequency.

Further experimental results on the parity of the nonlinear effects, the experimental uncertainties and the SI-GaAs spectrum are reported in Secs. VI–VIII [21]. Additional TDS simulations of the NL effects using only impact ionization as the carrier generation mechanism as a function of temperature and  $E_1$  peak field amplitude are shown in Sec. IX [21].

#### IV. DISCUSSION

In the 1D-TDS measurements, the overall decrease in transmission with increasing temperature seen in Fig. 1 has been explained in earlier work as the result of an increase in the density of thermally activated carriers, a conclusion that

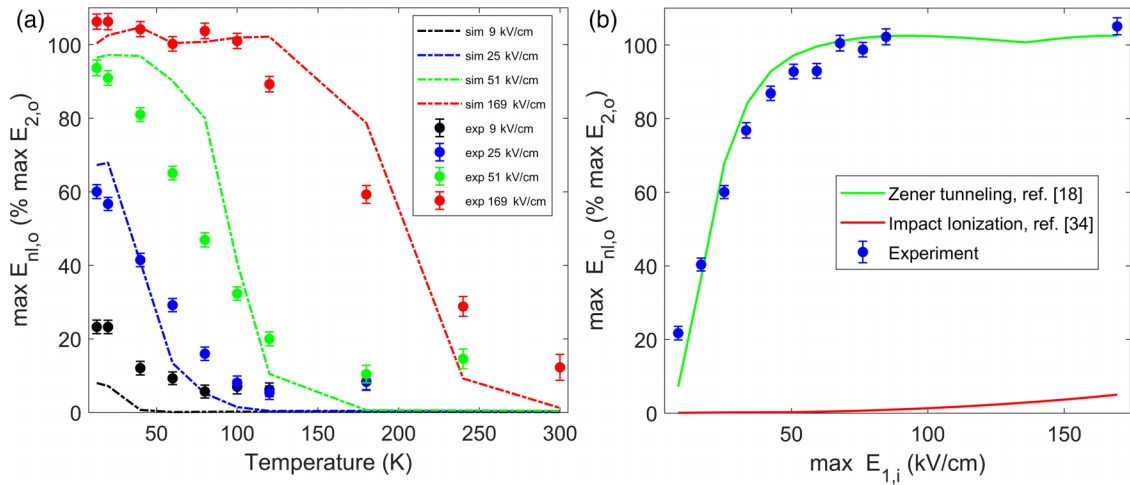


FIG. 4. Peak amplitudes of the nonlinear effects observed at  $t_{\text{ex}} = 2.54$  ps (averaged around a  $\pm 67$  fs range). (a) Experimental and simulated temperature dependence at selected fields (b) Experimental and simulated field dependence at  $T = 20$  K employing different carrier generation mechanisms.

is consistent with our simulation results (Refs. [10,39] and Sec. III [21]).

Counter to this trend, a small increase in the transmission was detected from 13 to 60 K between 1 and 2 THz. This is reproduced by the simulations, and appears to be connected with a reduction of the electronic damping parameter  $\gamma_p$ . This may indicate a decrease of the scattering pathways due to the opening of the band gap [44].

Now we turn to the discussion of the nonlinear 2D data shown in Figs. 2 and 3. Around the region of the temporal superposition between the two pulses, we observe oscillations in the nonlinear signal which, from the comparison between experiments and simulations, we attribute to quasiballistic motion of the carriers. At low temperature, the nonlinear response rapidly reaches a plateau mainly linked to carrier generation effects. The larger carrier concentration causes a reduced transmission of pulse 2 after the arrival of pulse 1. From a comparison between the two carrier generation models shown in Fig. 4(b), we identify the predominant mechanism

as Zener tunneling [18]. Besides reducing the transmission of pulse 2, carrier generation also changes the spectral content of the transmitted field. As seen in Fig. 5, at higher peak fields of pulse 1, the average period of the transmitted portion of pulse 2 is markedly smaller, suggesting that the higher carrier concentration filters out low frequencies preferentially. This is consistent with the data of Fig. 1, where we see that as carrier concentration increases with temperature, lower frequencies are more attenuated. This is even evident in the times when the pulses overlap, as shown in Fig. 3(a) where we show the low- and high-field nonlinear signal at  $T = 20$  K as a function of excitation delay. Here we see that for higher peak field values the periodicity of the modulation decreases, suggesting that here as well lower frequency components are attenuated more strongly as carriers are generated.

For higher sample temperatures, carrier generation processes are strongly reduced due to the increase of the band gap [10] [Figs. 4(a) and 4(b)]. As a result, the nonlinear signal for short excitation delay ranges is determined by the ballistic

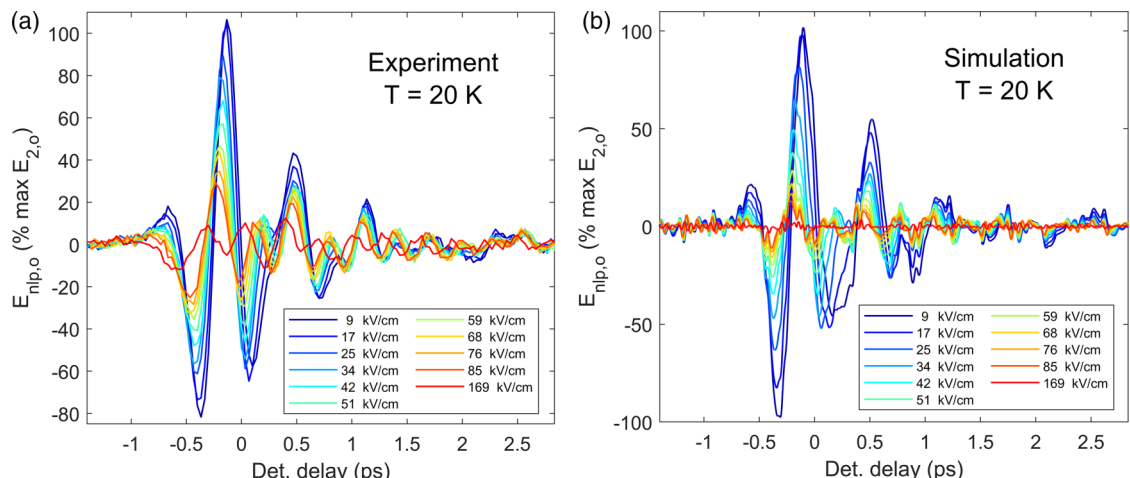


FIG. 5. (a) Experimental and (b) FDTD-simulated peak  $E_{1,i}$  field dependence of  $E_{\text{nlp},o}$  acquired at  $t_{\text{ex}} = 2.54$  ps averaged around a  $\pm 67$  fs range at  $T = 20$  K.

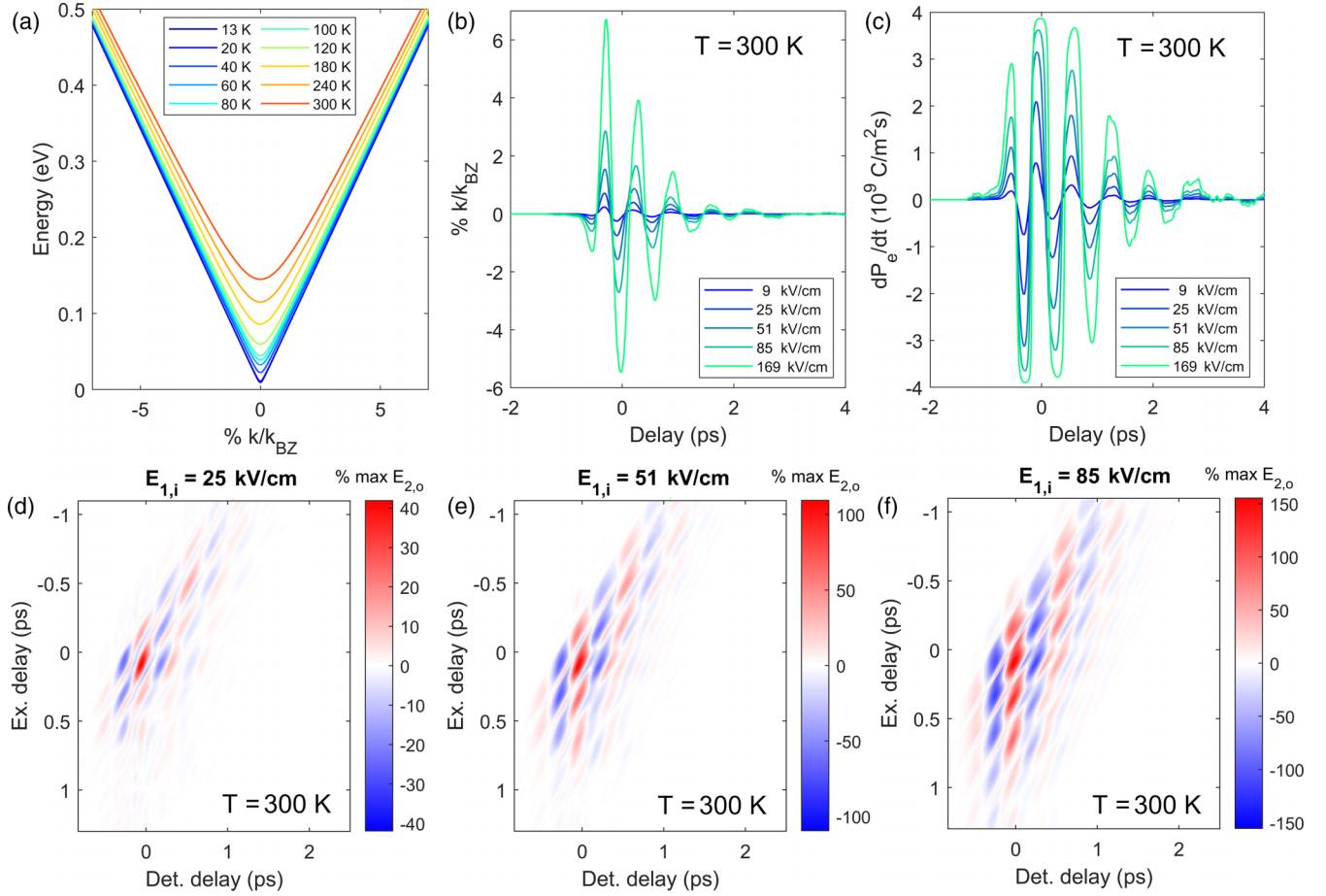


FIG. 6. (a) Conduction band using the parameters used for the FDTD simulations. (b) Simulated reciprocal space excursion of the electron wavepacket using  $E_1$  single pulses of different field amplitudes. (c) Simulated temporal derivative of the electronic polarization for different field amplitudes. For the last two panels, the results refer to the first simulation cell of the  $\text{Hg}_{0.825}\text{Cd}_{0.175}\text{Te}$  layer. [(d)–(f)] Simulated field dependence of  $E_{nl,o}$  at  $T = 300$  K and peak  $E_{2,i} = 8$  kV/cm.

response and confined to the times when the pulses overlap. In contrast to the nonlinear signal at low temperatures, at high temperatures the sign of the nonlinearity indicates a transient *increase* in the transmission of pulse 2.

The source of the nonlinearities for the ballistic response comes from the differences in the dynamics of the electronic polarization among the different combinations of the two pulses. In fact, the rate of change in the polarization density, described by Eq. (3), is proportional to the velocity  $\mathbf{v}[\mathbf{k}(t)]$ , which strongly depends on the history of the time-dependent interaction between electron wavepacket and electric field up to the instant  $t$  [Eqs. (4) and (6)]. Thus the ballistic nonlinear signal can occur in temporal regions where the evolution  $\mathbf{v}[\mathbf{k}(t)]$  is significantly altered by the simultaneous application of the two pulses rather than it being simply the sum of the trajectories in reciprocal space given by the two individual pulses. Moreover, the rate described by Eq. (3) is proportional to the carrier density  $n$ , favoring the higher temperatures which possess a larger carrier concentration. There are, however, other changes that occur with an increase in temperature that affect the ballistic nonlinearities. These variations are a consequence of modifications to the conduction band dispersion as the temperature increases (Fig. 6(a) and Refs. [10,14]). According to Eq. (6), an increase in the amplitude of the local

electric field  $\mathbf{E}$  will translate into a proportional increase in the amplitude of oscillations in the momentum space. In Fig. 6(b), we show a simulation of the dynamics of the wave-packet wave vector  $k$  as a function of pulse 1 peak amplitude that confirms this relationship. The level of the nonlinear response, however, is determined not by the change of the momentum  $k$ , but by the variations in the time derivative of the electronic polarization density  $P_e$ , which is, according to Eq. (3), proportional to the group velocity of the wave packet. This leads to a saturation of the electronic polarization density for high driving fields, as shown in Fig. 6(c) due to the peculiar, asymptotically linear, conduction dispersion [Eq. (5)]. As a result, ballistic nonlinearities with close magnitude occur over a wider range of excitation delays than the temporal profile of pulse 1 might suggest, as shown by the simulated 2D-TDS nonlinear signal in Figs. 6(d)–6(f), obtained by varying the peak amplitude of the incident field  $E_{1,i}$ .

As shown in Fig. 6(a), the saturation of the group velocity occurs much closer to the  $\Gamma$  point as the temperature decreases. Therefore one would expect saturation effects in ballistic nonlinearities to occur at lower field amplitudes at low temperature. In reality, in such conditions the nonlinear response is heavily influenced by carrier generation processes. This limits the visibility of these features at low temperatures.



In absence of carrier generation, we would expect indeed a very strong dependence of the ballistic nonlinearities on the band structure, as shown though further simulations in Sec. X [21].

The slower, approximately 1-ps timescale dynamics present at high temperature [Figs. 2(h) and 3(b)], is semi-quantitatively reproduced by our simulations [Fig. 2(i)] by considering ballistic transport. A similar increase in the transmission could be in principle caused by direct or assisted intervalley scattering towards the neighboring  $L$  and  $X$  valleys, depending on how far the electrons travel from the bottom of the  $\Gamma$  valley. This was shown to occur in similar zinc-blende compounds [45,46]. In this scenario, the increase in transmission is determined by the fact that electron mobility is much lower in the neighboring valleys due to the larger effective mass, leading to a reduction of the equilibrium plasma frequency. In the literature, tight-binding band structures calculated for different alloy compositions [47] suggest that a high ( $> 1$  eV) barrier electron energy is required, while density functional theory simulations for HgTe suggest a lower threshold ( $\approx 0.5$  eV) [48]. From our simulations, the peak energy acquired by the electrons at 300 K under pulses with peak field amplitude of 169 kV/cm is not sufficient ( $< 0.5$  eV) to escape from the  $\Gamma$  valley. This suggests that a strong contribution by intervalley scattering is unlikely in our case.

At sufficiently long time scales, we expect the electrons to return gradually to the bottom of the  $\Gamma$  valley, thermalize and recombine with holes of the valence bands mainly through Shockley-Read-Hall, Auger recombination or radiative decay [47,49]. This and other slower changes in the conduction band occupation may explain the slow dynamics in  $E_{\text{nlp,o}}$  as a function of excitation delay seen at high peak fields (Sec. V [21]). Excitation and relaxation phenomena over such a time scale have a key role in determining the response and design of very-long wavelength detectors based on the material, where the control of generation and scattering processes is central [50,51].

While capturing many of the main features of the nonlinear response, our simulations have some limitations. One arises from treating the entire carrier population as a single electron wave packet, instead of an ensemble via, for example, a Monte Carlo treatment [52]. This is a practical trade-off: ensemble treatments are much more computationally intensive, and would be difficult to include in our simulations. An ensemble-based simulation would broaden the velocity distribution of the particles. This might cause a smearing-out of the oscillations seen for times corresponding to the overlap of the pulses closer to the experimental results [Figs. 2(h), 2(i) and 3(b)].

As noted above, based on a comparison of our simulations with the experiment, we conclude that Zener tunneling is the dominant carrier generation process. One approach to discuss the validity of our model of Zener tunneling is to consider the Keldysh parameter  $\gamma_K = 2\pi\nu_0\sqrt{2m_e\mathcal{E}_g}/(eE)$ , where  $\nu_0$  is the light frequency,  $m_e$  is the electron mass,  $\mathcal{E}_g$  is the energy gap,  $e$  the fundamental charge and  $E$  the electric field magnitude [31,53,54]. Strictly speaking our treatment of Zener tunneling assumes  $\gamma_K \ll 1$ . In MCT at  $T = 13$  K (where the gap is within the bandwidth of the THz pulse), the Keldysh parameter becomes unitary around 40 kV/cm for  $\nu_0 = 2$  THz. This

suggests that we may be approaching the limits of validity for the Zener tunneling model at the lowest temperatures using low field amplitudes. Extensions and corrections to the original Zener derivation have been proposed by several authors [18,32,33,55,56] that may improve agreement. For example, the extension proposed by Bhan and Gopal [33] effectively reduces the contribution of carrier generation at high fields and could improve the field dependence of the nonlinear signal. To lift the low-field approximation, the model provided by Ishikawa for 2D graphene [57] could provide a more general framework if adapted to include a very small effective mass. Furthermore, a revised model could also in principle take into account the effects of having carriers already in the conduction band.

Despite our conclusion that we do not see evidence of significant impact ionization in our experiment, it has been reported to occur in quantum wells containing HgCdTe both for much longer, approximately 100 ns, THz pulses and in experiments using a static electric field bias [34,58,59]. We believe that in these works impact ionization is more significant due to the much longer pulse (or field application) duration and more moderate electric fields, which combine to dramatically enhance the influence of impact ionization relative to that of Zener tunneling. A qualitative simulation of this is presented in Sec. XI, [21].

Lastly, we consider the possibility that the CdTe and ZnTe buffer layers and GaAs substrate may contribute to the observed nonlinearity. These materials are larger-gap semiconductors (1.5 eV for CdTe, 2.3 eV for ZnTe, and 1.5 eV for GaAs) compared to our MCT sample (Ref. [60]) and are nominally semi-insulating [20]. While reports have shown that it is possible to induce nonlinearities in  $n$ -doped GaAs at field amplitudes comparable to the ones used in our experiment, on SI-GaAs this has shown to be feasible only through a large local field enhancement using metallic structures [61–63]. We therefore rule out a major contribution to the nonlinear signal coming from those layers. Furthermore, the transmission spectrum of SI-GaAs is only weakly temperature-dependent in our frequency window as reported in Sec. VIII [21].

## V. CONCLUSIONS

We have shown how the band gap, carrier concentration and band shape intertwine to determine the carrier dynamics in the narrow-gap semiconductor  $\text{Hg}_{0.825}\text{Cd}_{0.175}\text{Te}$  and how they heavily affect the nonlinear response of the material to transient THz fields. At low temperature, where the band gap is small, the initially ballistic dynamics leads to carrier generation mainly via Zener tunneling, which dominates the nonlinear response. At high temperature, under a higher carrier concentration, larger band gap and more parabolic-like band shape, a pronounced nonlinear ballistic response confined around the temporal overlap region of the two pulses was observed while carrier generation is heavily suppressed. Moreover, these phenomena influence the carrier dynamics over tens of picoseconds, which in turn impact the response and design of very-long wavelength detectors based on the material. The nonlinear response to ultrafast pulses is therefore seen to depend strongly on experimental parameters such as temperature, carrier concentration and field amplitude.

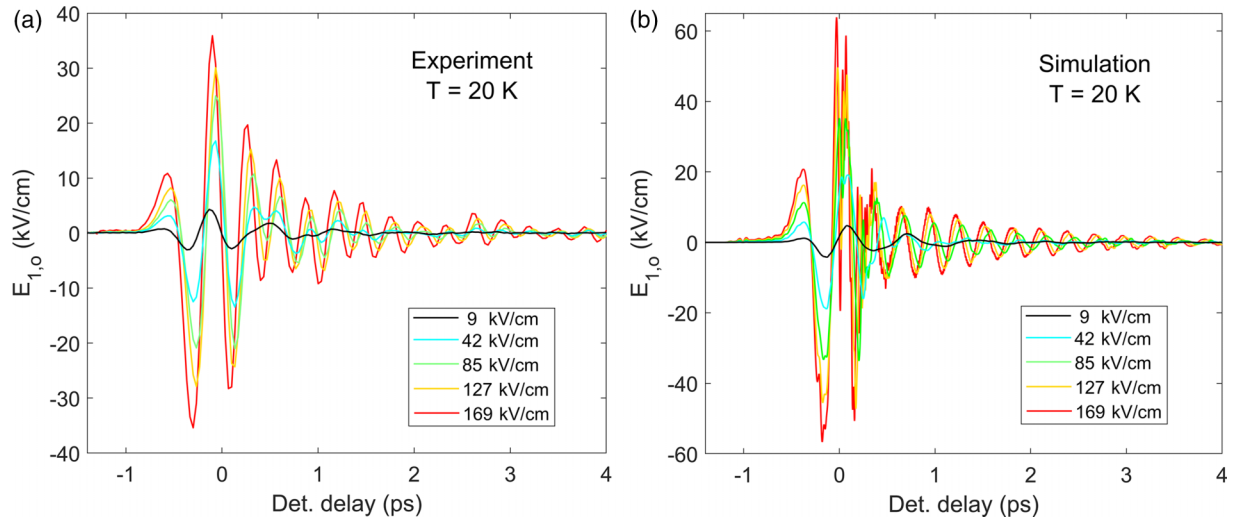


FIG. 7. (a) Experimental and (b) simulated peak  $E_{1,i}$  field amplitude dependence of the transmitted  $E_{1,o}$  pulse through the MCT multilayer at  $T = 20$  K.

While the present work is based on MCT, the key concepts presented here can be easily extended to analogous narrow-gap semiconductors.

#### ACKNOWLEDGMENTS

This work was supported by the Swiss National Science Foundation under Project No. 200020\_192337. E.A. acknowledges funding support from the Swiss National Science Foundation through Ambizione Grant No. PZ00P2\_179691 and through Starting Grant TMSGI2\_211211. This work was also supported by the CNRS through IRP “TeraMIR” and by the “ANR” for Equipex+ Hybat project (ANR-21 -ESRE-0026). High-performance computing resources were obtained from ETH Zürich (Euler cluster).

#### APPENDIX: INTRAPULSE DYNAMICS

In Fig. 7(a), we report the experimental time-domain trace of the transmitted  $E_{1,o}$  pulse. Here the input field amplitude was varied by rotating the first of a pair of wire-grid polarizers,

which causes a frequency-independent attenuation. For comparison, panel (b) shows the corresponding simulated data.

The spectral shape of the transmitted  $E_{1,o}$  field shows clear differences on varying the input field amplitude. Similar effects occur in semiconductors like  $n$ -doped GaAs, where it has been attributed to self-phase modulation from carrier generation during the pulse [64]. The first oscillations of the terahertz pulse are enough to lead to a considerable increase in the carrier population which in turn influence the transmission of the following part of the pulse. This is why for the first one or two oscillations the difference between the waveforms is well-approximated as a simple rescaling of the amplitude, whereas the rest of the transmitted pulse appears to have a higher frequency, due to the spectral filtering effect of the increased carrier density discussed in the main text. The presence of sudden spikes in correspondence of the highest field amplitudes, around  $t_{\text{del}} \approx 0$  ps in panel (b), is connected to the limitations of our FDTD algorithm and the single electron wave-packet approximation instead of an electronic ensemble.

- 
- [1] J. Wang, S. Deng, Z. Liu, and Z. Liu, *Natl. Sci. Rev.* **2**, 22 (2015).
- [2] N. P. Armitage, E. J. Mele, and A. Vishwanath, *Rev. Mod. Phys.* **90**, 015001 (2018).
- [3] S. Tani, F. Blanchard, and K. Tanaka, *Phys. Rev. Lett.* **109**, 166603 (2012).
- [4] P. Bownan, E. Martinez-Moreno, K. Reimann, T. Elsaesser, and M. Woerner, *Phys. Rev. B* **89**, 041408(R) (2014).
- [5] M. Baudisch, A. Marini, J. D. Cox, T. Zhu, F. Silva, S. Teichmann, M. Massicotte, F. Koppens, L. S. Levitov, F. J. García de Abajo, and J. Biegert, *Nat. Commun.* **9**, 1018 (2018).
- [6] P. R. Norton, *Opto-Electron. Rev.* **10**, 159 (2002).
- [7] W. Lei, J. Antoszewski, and L. Faraone, *Appl. Phys. Rev.* **2**, 041303 (2015).
- [8] R. Dornhaus and G. Nimtz, The properties and applications of the  $\text{Hg}_{1-x}\text{Cd}_x\text{Te}$  alloy system, in *Solid-State Physics* (Springer, Berlin, Heidelberg, 1976), pp. 1–119.
- [9] E. O. Kane, in *Narrow Gap Semiconductors Physics and Applications* (Springer, Berlin, Heidelberg, 1980), pp. 13–31.
- [10] F. Teppe, M. Marcinkiewicz, S. S. Krishtopenko, S. Ruffenach, C. Consejo, A. M. Kadykov, W. Desrat, D. But, W. Knap, J. Ludwig, S. Moon, D. Smirnov, M. Orlita, Z. Jiang, S. V. Morozov, V. I. Gavrilenko, N. N. Mikhailov, and S. A. Dvoretiskii, *Nat. Commun.* **7**, 12576 (2016).
- [11] C. Brüne, C. X. Liu, E. G. Novik, E. M. Hankiewicz, H. Buhmann, Y. L. Chen, X. L. Qi, Z. X. Shen, S. C. Zhang, and L. W. Molenkamp, *Phys. Rev. Lett.* **106**, 126803 (2011).

- [12] M. Szoła, Y. Ivonyak, J. Przybytek, N. Mikhailov, S. Dvoretzky, F. Teppe, and W. Knap, *Phys. Rev. B* **106**, 195202 (2022).
- [13] S. S. Krishtopenko, M. Antezza, and F. Teppe, *Phys. Rev. B* **106**, 115203 (2022).
- [14] M. Orlita, D. M. Basko, M. S. Zholudev, F. Teppe, W. Knap, V. I. Gavrilenko, N. N. Mikhailov, S. A. Dvoretzky, P. Neugebauer, C. Faugeras, A.-L. Barra, G. Martinez, and M. Potemski, *Nat. Phys.* **10**, 233 (2014).
- [15] S. S. Krishtopenko and F. Teppe, *Phys. Rev. B* **105**, 125203 (2022).
- [16] W. Kuehn, K. Reimann, M. Woerner, and T. Elsaesser, *J. Chem. Phys.* **130**, 164503 (2009).
- [17] K. Yee, *IEEE Trans. Antennas Propag.* **14**, 302 (1966).
- [18] E. Kane, *J. Phys. Chem. Solids* **12**, 181 (1960).
- [19] C. L. Dick and B. Ancker-Johnson, *Phys. Rev. B* **5**, 526 (1972).
- [20] S. Dvoretzky, N. Mikhailov, V. Remesnik, Y. Sidorov, V. Shvets, D. Ikusov, V. Varavin, M. Yakushev, J. Gumenjuk-Sichevska, A. Golenkov, I. Lysiuk, Z. Tsybrii, A. Shevchik-Shekera, F. Sizov, A. Latyshev, and A. Aseev, *Opto-Electron. Rev.* **27**, 282 (2019).
- [21] See Supplemental Material at <http://link.aps.org/supplemental/10.1103/PhysRevB.110.094303> for additional details on the sample, experimental data and simulation results, which includes Refs. [65–69].
- [22] T. Suter, A. Tomasino, M. Savoini, S. Houver, R. Morandotti, S. L. Johnson, and E. Abreu, *Opt. Express* **30**, 45202 (2022).
- [23] C. Vicario, M. Jazbinsek, A. V. Ovchinnikov, O. V. Chefonov, S. I. Ashitkov, M. B. Agranat, and C. P. Hauri, *Opt. Express* **23**, 4573 (2015).
- [24] H. Hirori, A. Doi, F. Blanchard, and K. Tanaka, *Appl. Phys. Lett.* **98**, 091106 (2011).
- [25] K. Reimann, *Rep. Prog. Phys.* **70**, 1597 (2007).
- [26] L. Huber, Ph.D. thesis, ETH Zurich, Zurich, 2017.
- [27] R. C. Rumpf, *Electromagnetic and Photonic Simulation for the Beginner: Finite-Difference Frequency-Domain in MATLAB®* (Artech House, Norwood, 2022).
- [28] S. Houver, L. Huber, M. Savoini, E. Abreu, and S. L. Johnson, *Opt. Express* **27**, 10854 (2019).
- [29] S. Yu, K. H. Heffernan, and D. Talbayev, *Phys. Rev. B* **95**, 125201 (2017).
- [30] M. C. Hoffmann, J. Hebling, H. Y. Hwang, K.-L. Yeh, and K. A. Nelson, *Phys. Rev. B* **79**, 161201(R) (2009).
- [31] Y. Sanari, T. Tachizaki, Y. Saito, K. Makino, P. Fons, A. V. Kolobov, J. Tominaga, K. Tanaka, Y. Kanemitsu, M. Hase, and H. Hirori, *Phys. Rev. Lett.* **121**, 165702 (2018).
- [32] C. Zener and R. H. Fowler, *Proc. R. Soc. London A* **145**, 523 (1934).
- [33] R. K. Bhan and V. Gopal, *Semicond. Sci. Technol.* **9**, 289 (1994).
- [34] M. A. Kinch, in *Fundamentals of Infrared Detectors* (SPIE Publications, 2007), Chap. 7.
- [35] M. B. Reine, Semiconductor materials, mercury cadmium telluride, in *Encyclopedia of Modern Optics* (Elsevier, Berlin, Heidelberg, 2005), pp. 392–402.
- [36] J. Baars and F. Sorger, *Solid State Commun.* **10**, 875 (1972).
- [37] S. Biasco, F. Burri, S. Houver, E. Abreu, M. Savoini, and S. L. Johnson, *Phys. Rev. B* **106**, 235201 (2022).
- [38] W. Zawadzki, *Adv. Phys.* **23**, 435 (1974).
- [39] M. Grynberg, R. Le Toullec, and M. Balkanski, *Phys. Rev. B* **9**, 517 (1974).
- [40] J. Polit, E. M. Sheregii, J. Cebulski, A. Kisiel, B. V. Robouch, A. Marcelli, and A. Mycielski, *Phys. Rev. B* **82**, 014306 (2010).
- [41] S. P. Kozyrev, *Phys. Solid State* **53**, 163 (2011).
- [42] P. M. Amirtharaj, N. K. Dhar, J. Baars, and H. Seelewind, *Semicond. Sci. Technol.* **5**, S68 (1990).
- [43] S. P. Kozyrev, L. K. Vodopyanov, and R. Triboulet, *Phys. Rev. B* **58**, 1374 (1998).
- [44] Y. Chang, G. Badano, J. Zhao, Y. D. Zhou, R. Ashokan, C. H. Grein, and V. Nathan, *J. Electron. Mater.* **33**, 709 (2004).
- [45] I.-C. Ho and X.-C. Zhang, *Front. Optoelectron.* **7**, 220 (2014).
- [46] S. Ašmontas, S. Bumelienė, J. Gradauskas, R. Raguotis, and A. Sužiedėlis, *Sci. Rep.* **10**, 10580 (2020).
- [47] C. R. Becker and S. Krishnamurthy, Band structure and related properties of HgCdTe, in *Mercury Cadmium Telluride* (John Wiley & Sons, Ltd, 2010), Chap. 12, pp. 275–295.
- [48] W. Feng, D. Xiao, Y. Zhang, and Y. Yao, *Phys. Rev. B* **82**, 235121 (2010).
- [49] V. Y. Aleshkin, V. V. Rumyantsev, K. E. Kudryavtsev, A. A. Dubinov, V. V. Utochkin, M. A. Fadeev, G. Alymov, N. N. Mikhailov, S. A. Dvoretzky, F. Teppe, V. I. Gavrilenko, and S. V. Morozov, *J. Appl. Phys.* **129**, 133106 (2021).
- [50] Q. Li, R. Xie, F. Wang, S. Liu, K. Zhang, T. Zhang, Y. Gu, J. Guo, T. He, Y. Wang, P. Wang, Y. Wei, and W. Hu, *Opt. Express* **30**, 16509 (2022).
- [51] L. Wehmeier, M. Liu, S. Park, H. Jang, D. N. Basov, C. C. Homes, and G. L. Carr, *ACS Photonics* **10**, 4329 (2023).
- [52] K. F. Brennan and N. S. Mansour, *J. Appl. Phys.* **69**, 7844 (1991).
- [53] L. V. Keldysh, *Zh. Eksp. Teor. Fiz.* **47**, 1945 (1965) [*J. Exp. Theor. Phys.* **20**, 1307 (1965)].
- [54] C. Lange, T. Maag, M. Hohenleutner, S. Baierl, O. Schubert, E. R. J. Edwards, D. Bougeard, G. Woltersdorf, and R. Huber, *Phys. Rev. Lett.* **113**, 227401 (2014).
- [55] L. Fritsche, *Phys. Status Solidi B* **13**, 487 (1966).
- [56] P. Chakraborty and J. Biswas, *Solid-State Electron.* **28**, 493 (1985).
- [57] K. L. Ishikawa, *Phys. Rev. B* **82**, 201402(R) (2010).
- [58] G. J. Rees and J. P. R. David, *J. Phys. D* **43**, 243001 (2010).
- [59] S. Hubmann, S. Gebert, G. V. Budkin, V. V. Bel'kov, E. L. Ivchenko, A. P. Dmitriev, S. Baumann, M. Otteneder, J. Ziegler, D. Disterheft, D. A. Kozlov, N. N. Mikhailov, S. A. Dvoretzky, Z. D. Kvon, D. Weiss, and S. D. Ganichev, *Phys. Rev. B* **99**, 085312 (2019).
- [60] S. Kasap and P. Capper, *Springer Handbook of Electronic and Photonic Materials* (Springer, Berlin, 2006).
- [61] H. Hirori, K. Shinokita, M. Shirai, S. Tani, Y. Kadoya, and K. Tanaka, *Nat. Commun.* **2**, 594 (2011).
- [62] K. Fan, H. Y. Hwang, M. Liu, A. C. Strikwerda, A. Sternbach, J. Zhang, X. Zhao, X. Zhang, K. A. Nelson, and R. D. Averitt, *Phys. Rev. Lett.* **110**, 217404 (2013).
- [63] D. Kim, D.-S. Kim, and G. Choi, *APL Photonics* **8**, 036107 (2023).
- [64] D. Turchinovich, J. M. Hvam, and M. C. Hoffmann, *Phys. Rev. B* **85**, 201304(R) (2012).

- [65] M. Schall, M. Walther, and P. U. Jepsen, *Phys. Rev. B* **64**, 094301 (2001).
- [66] W. J. Moore and R. T. Holm, *J. Appl. Phys.* **80**, 6939 (1996).
- [67] G. L. Hansen, J. L. Schmit, and T. N. Casselman, *J. Appl. Phys.* **53**, 7099 (1982).
- [68] I. Katayama, H. Kawakami, T. Hagiwara, Y. Arashida, Y. Minami, L.-W. Nien, O. S. Handegard, T. Nagao, M. Kitajima, and J. Takeda, *Phys. Rev. B* **98**, 214302 (2018).
- [69] J. Fornies-Marquina, J. Letosa, M. Garcia-Gracia, and J. Artacho, *IEEE Trans. Magn.* **33**, 1456 (1997).